Arabian Journal of Chemistry (2020) **13**, 3043–3059

King Saud University

Arabian Journal of Chemistry

www.ksu.edu.sa
www.sciencedirect.com

ORIGINAL ARTICLE

Mechanistic roles of substitutional Fe dopants on catalytic acetylene-sensing process of flame-made SnO_2 nanoparticles

Jirasak Sukunta [a,b], Anurat Wisitsoraat [c,d,e], Adisorn Tuantranont [c,f], Kata Jaruwongrungsee [d], Sukon Phanichphant [c], Chaikarn Liewhiran [a,c,g,*]

[a] *Department of Physics and Materials Science, Faculty of Science, Chiang Mai University, Chiang Mai 50200, Thailand*
[b] *Graduate School, Chiang Mai University, Chiang Mai 50200, Thailand*
[c] *Center of Advanced Materials for Printed Electronics and Sensors, Materials Science Research Center, Faculty of Science, Chiang Mai University, Chiang Mai 50200, Thailand*
[d] *Carbon-based Devices and Nanoelectronics Laboratory, National Electronics and Computer Technology Center, National Science and Technology Development Agency, Klong Luang, Pathumthani 12120, Thailand*
[e] *Department of Common and Graduate Studies, Sirindhorn International Institute of Technology, Thammasat University, Pathumthani 12120, Thailand*
[f] *Thailand Organic and Printed Electronics Innovation Center, National Electronics and Computer Technology Center, National Science and Technology Development Agency, Klong Luang, Pathumthani 12120, Thailand*
[g] *Center of Excellence in Materials Science and Technology, Chiang Mai University, Chiang Mai 50200, Thailand*

Received 8 June 2018; accepted 23 August 2018
Available online 31 August 2018

KEYWORDS

Fe doping;
SnO_2;
Flame spray pyrolysis;
Metal oxide;
Acetylene;
Gas sensor

Abstract In this work, flame-spray-made Fe-doped SnO_2 nanoparticles were comprehensively investigated for acetylene (C_2H_2) detection and the roles of Fe dopants on sensing mechanisms were explored. The sensing material properties were evaluated by X-ray diffraction, electron microscopy, N_2 adsorption-desorption analysis, X-ray absorption/photoemission spectroscopy and UV–visible spectroscopy. The structural characterizations confirmed that the nanoparticles had a tetragonal nanocrystalline SnO_2 phase and Fe^{3+} dopant species formed a solid solution with SnO_2 lattice. The sensors were measured towards 0.15–3 vol% C_2H_2 in dry air at various working temperatures (200–350 °C). Gas-sensing data demonstrated that the optimal Fe doping level of 0.1 wt% led to a substantially enhanced response of 748.7 toward 3 vol% C_2H_2 with a decent response time of 2.5 s at the optimal working temperature of 300 °C. Furthermore, the optimal SnO_2 sensor demonstrated

* Corresponding author at: Department of Physics and Materials Science, Faculty of Science, Chiang Mai University, Chiang Mai 50200, Thailand.
E-mail address: cliewhiran@gmail.com (C. Liewhiran).
Peer review under responsibility of King Saud University.

Production and hosting by Elsevier

https://doi.org/10.1016/j.arabjc.2018.08.013

high C_2H_2 selectivity against C_2H_5OH, NO_2, H_2, NH_3, CO_2, NO, H_2S, CH_4, C_2H_4O, C_2H_4 and N_2O. Additional detailed analyses suggested that Fe^{3+} species played catalytic roles for enhancing C_2H_2 dissociation and oxidation. Thus, the Fe-doped SnO_2 sensors were highly promising for selective and sensitive detections of acetylene in industrial applications.

1. Introduction

Semiconducting metal oxide gas sensors have been utilized extensively in various industrial applications owing to their relatively low cost and long life compared with other gas-sensing technologies. Most metal oxides are suitable to detect harmful, toxic, flammable and environmental gases while some others may be used in specific applications such as medical breath diagnosis, foods quality analysis and so on (Righettoni et al., 2010). Thus, the new metal oxide materials and nanostructures have been continually developed to attain excellent sensitivity, outstanding selectivity, fast response/recovery rate and long-term stability for practical use. Among various metal oxides, tin oxide (SnO_2) has still been the most effective gas-sensitive material due to its broad gas response, modest conductivity, good stability and low price. Moreover, its gas-sensing performances including sensitivity, selectivity and operating temperature can be extensively tailored by various modification techniques including doping, loading, compositing, core-shell formation and other nanostructural processing. Doping with reactive transition metals including iron (Fe), nickel (Ni) and cobalt (Co) is one of the most successful strategies to improve the response and specificity to a target gas. Among these, Fe and Fe_2O_3 are particularly attractive additives for SnO_2 because of its useful catalytic activity and low cost. The gas-sensing behaviors of SnO_2 nanostructures with Fe or Fe_2O_3 additives prepared by different methods have been extensively studied as registered in Table 1. For instance, the SnO_2/Fe_2O_3 double-layer thin film deposited by a sol-gel method exhibits an enhanced response of 19.8–1000 ppm ethanol at 250 °C (Jiao et al., 2000). Similarly, core–shell Fe_2O_3@SnO_2 nanohybrids made by flame-assisted spray pyrolysis offer a superior response of 22.8–100 ppm ethanol at 300 °C (Li et al., 2013). Also, Fe_2O_3 nanoparticle-coated SnO_2 nanowires fabricated

Table 1 Gas-sensing characteristics of $Fe/FeO_x - SnO_2$ materials synthesized by various techniques.

Sensing materials	Methods	Sensing performances			Ref.
		Concentrations	Response/ t_{res}	Temp.	
SnO_2/Fe_2O_3 multilayer thin film	Sol-gel	1000 ppm C_2H_5OH	19.8/–	250 °C	Jiao et al. (2000)
Core–shell Fe_2O_3@SnO_2 nanohybrids	Flame-assisted spray pyrolysis	100 ppm C_2H_5OH	22.8/–	300 °C	Li et al. (2013)
Fe_2O_3 nanoparticles-coated SnO_2 nanowires	VLS and hydrothermal	200 ppm C_2H_5OH	57.6/65 s	300 °C	Choi et al. (2017)
Hierarchical α-Fe_2O_3/SnO_2 composites	Hydrothermal	100 ppm C_3H_6O 100 ppm C_2H_5OH	16.8/– 7.2/–	250 °C	Sun et al. (2013)
Porous core–shell α-Fe_2O_3@SnO_2 nanotubes	Hydrothermal	100 ppm C_3H_6O	33.4/–	300 °C	Yu et al. (2015)
SnO_2–Fe_2O_3 interconnected nanotubes	Electrospinning and thermal treatment	50 ppm Toluene	25.3/–	260 °C	Shan et al. (2013)
α-Fe_2O_3/SnO_2 nanorod composites	Hydrothermal	1% LPG	32/ < 5 s	370 °C	Vuong et al. (2014)
Hollow SnO_2 sphere	Hydrothermal and calcination	100 ppm C_2H_2	5.4/6 s	206 °C	Lin et al. (2015)
NiO/SnO_2 heterostructure			13.8/2 s		
SnO_2 nanoparticles	Flame spray pyrolysis	1 vol% C_2H_2	6.3/34 s	300 °C	Liewhiran et al. (2012)
Pd-doped SnO_2 nanoparticles	Hydrothermal	100 μL/L C_2H_2	7.22/–	350 °C	Chen et al. (2013a)
SnO_2 nanowire	Hydrothermal	100 μL/L C_2H_2	46.96/7 s	250 °C	Chen et al. (2013b)
SnO_2 nanorod			34.04/11 s		
SnO_2 nanosphere			26.80/13 s	280 °C	
SnO_2 nanobulk			20.34/15 s		
SnO_2	Sol–gel	1000 ppm C_2H_2	3.8/–	180 °C	Qi et al. (2008)
Sm_2O_3-doped SnO_2			63.8/5 s		
SnO_2	Hydrothermal	50 μL/L C_2H_2	7.53/8–10 s	260 °C	Zhou et al. (2015)
Sm_2O_3 decorated SnO_2			38.12/8–10 s		
Fe_2O_3-doped SnO_2 nanoparticles	Flame spray pyrolysis and spin coating	3 vol% C_2H_2	748/~2.5 s	300 °C	This work

by vapor-liquid-solid (VLS) and hydrothermal processes provide a decent response of 57.6–200 ppm ethanol at 300 °C (Choi et al., 2017). Differently, hierarchical α-Fe_2O_3/SnO_2 composites and porous core–shell α-Fe_2O_3@SnO_2 nanotubes synthesized by hydrothermal routes display selective responses of 16.8 and 33.4–100 ppm acetone at 250 °C (Sun et al., 2013) and 300 °C (Yu et al., 2015), respectively. Moreover, SnO_2–Fe_2O_3 interconnected nanotubes produced by electrospinning and thermal treatment show a good response of 25.3–50 ppm toluene at 260 °C (Shan et al., 2013) while α-Fe_2O_3/SnO_2 nanorod composites give a decent response of 32–1% liquid petroleum gas (LPG) at 370 °C (Vuong et al., 2014). It is apparent that the impact of Fe/FeO_x on the gas-sensing properties of SnO_2 is substantially related to its preparation method, which dictates the surface and structural properties of the composite materials. Thus, the benefits of Fe/FeO_x doping can be better utilized by synthesizing superior Fe/FeO_x-doped SnO_2 nanostructures with an advanced preparation method.

Flame spray pyrolysis (FSP) is a highly attractive production method of metal-oxide sensing materials owing to large specific surface area of synthesized nano-sized metal oxide structures and homogeneous distribution of metal/metal oxide dopants (Liewhiran et al., 2012). Numerous SnO_2 nanoparticles incorporated with different transition metals including In, Co, Ni, Pd, Pt, V and Mo have been synthesized productively by FSP in a single step and reveal remarkable gas-sensing characteristics (Liewhiran et al., 2012, 2013; Sukunta et al., 2017; Punginsang et al., 2015; Singkammo et al., 2015). Nonetheless, there is still no report of Fe-doped SnO_2 gas-sensing materials produced by FSP. In this research, Fe-doped SnO_2 nanostructures are made by one-step FSP for the first time with different Fe doping concentrations and studied for gas-sensing properties towards diverse gases including C_2H_2, C_2H_5OH, NO_2, H_2, NH_3, CO_2, NO, H_2S, CH_4, C_2H_4O, C_2H_4 and N_2O. In addition, the role of Fe dopants on gas-sensing mechanisms are profoundly studied.

2. Experimental methods

2.1. Synthesis of metal-oxide nanoparticles

0–2 wt% Fe-doped SnO_2 nanostructures were made from a precursor mixture by the FSP system formerly developed by our research group (Liewhiran et al., 2012, 2013; Sukunta et al., 2017; Punginsang et al., 2015; Singkammo et al., 2015). Briefly, the precursor solution (0.50 M) was made by dissolving suitable amounts of tin (II) 2-ethylhexanoate (Aldrich, 95%) and iron (III) acetyl-acetonate (Aldrich, 99.9%) in the xylene solvent (CarloErba, 98.5%). In a nominal synthesis process, the precursor was injected into a FSP chamber using a syringe pump at 5 mL/min and then spread into droplets by O_2 flow (5 L/min) defined as the 5/5 flame condition with a fixed O_2 pressure of 1.5 bar. The spray was combusted by subsidiary flamelets formed with oxygen (2.46 L/min) and methane (1.19 L/min). A sheath O_2 flow of 3.92 L/min was applied coaxially about the nozzle to regulate and control the sprayed flame. SnO_2 nanoparticles were then nucleated after vaporization and incineration of the droplets followed by Fe-doping, coagulation and coalescence. Finally, nanoparticles were attracted with the use of vacuum onto a 25.7 cm-diameter microfiber glass filter (Whatmann GF/A). The unloaded SnO_2 powder was named as P-0 while doped SnO_2 powders with 0.1, 0.2, 0.5, 1 and 2 wt% Fe were labeled as P-0.1Fe, P-0.2Fe, P-0.5Fe, P-1Fe and P-2Fe, respectively.

2.2. Gas sensor fabrication

To form a paste for spin-coating of sensing films, as-prepared flame-made 0–2 wt% Fe-doped SnO_2 nanoparticles were meticulously mixed and crushed in a mortar with the binder solution (0.30 mL) containing ethyl cellulose (Fluka, 30–70 mPa s) and α-terpineol solvent (Aldrich, 90%) (Kotchasak et al., 2018). The obtained paste was deposited by spin-coating as a thick sensing film onto Au interdigitated electrodes prefabricated on an Al_2O_3 substrate (4 mm × 5.5 mm × 0.4 mm). The sensors were stabilized in a furnace at 450 °C for 3 h to completely remove binder. The sensors coated using P-0 to P-2Fe powder samples were consequently defined as S-0 to S-2Fe.

2.3. Particle and sensing film characterizations

The phase and crystallinity of the unloaded SnO_2 and 0.1–2 wt % Fe-doped SnO_2 nanoparticles and sensing films were assessed by X–ray diffraction in the glancing incident mode (GI-XRD) (Rigaku TTRAX III diffractometer) using CuK_α X-ray source (20 kV, 20 mA) scanned with a rate of 3°/min. The pore size distributions and specific surface areas of nanoparticles were measured by nitrogen adsorption, which was analyzed using Brunauer–Emmett–Teller (BET) and Barrett-Joyner-Halenda (BJH) methods. The structural morphologies of nanopowders and sensing films were inspected by high-resolution transmission electron microscopy (HR-TEM: JSM-2100Plus, JEOL) and scanning electron microscopy (SEM: JSM-6335F, JEOL). The oxidation states of iron in nanoparticles samples were evaluated by X-ray absorption spectroscopy (XAS) and X-ray photoemission spectroscopy (XPS). Moreover, the optical band gap energy of nanopowder was measured by UV–visible spectroscopy.

2.4. Gas-sensing measurement

The gas-sensing characteristics of Fe-doped SnO_2 sensors were evaluated towards C_2H_2, C_2H_5OH, NO_2, H_2, NH_3, CO_2, NO, H_2S, CH_4, C_2H_4O, C_2H_4 and N_2O at the atmospheric pressure in a closed stainless steel chamber having a dynamic volume of ~0.7 L. The sensors were tested by the typical flow through method at varying working temperatures from 200 to 350 °C controlled by an external dc-powered heater. In addition, the characteristics towards C_2H_2 as the main target gas were determined over the concentration range of 0.15–3 vol%. A flow of dry air as a carrier was delivered to combine with the designated concentration of gas sample balanced in dry air at a regular T-junction with a combined gas flow rate of 2 L/min. Computer-controlled mass flow controllers (5850E, Brook Instruments) were used to precisely regulate gas flow rates. The sensing devices were subjected to a target gas for 15 min at each concentration and the dry air flow was recovered for 35 min. The resistances of six sensors were simultaneously monitored at a constant bias of 10 V using a picoammeter (Keithley model 6487). The sensor response (S) was deter-

mined from R_a/R_g, where R_g was the steady-state resistance in a reducing gas (C_2H_5OH, H_2, NH_3, CO_2, H_2S, NO, CH_4, C_2H_4O and C_2H_4) and R_a was a baseline resistance in dry air. For oxidizing gas such as NO_2 and N_2O, the response function was inversed to R_g/R_a (Samerjai et al., 2012). The response time (t_{res}) was set as the time taken to reach 90% of the response signal and the recovery time (t_{rec}) was the time period to recover 90% of the baseline resistance.

3. Results and discussion

3.1. Structural characteristics of flame-made nanopowders and sensing films

XRD data of flame-made undoped and 0.1–2 wt% Fe-doped SnO_2 (P-0 and P-0.1Fe to P–2Fe) powders are reported in Fig. 1(a). It is apparent that sharp diffraction peaks of all

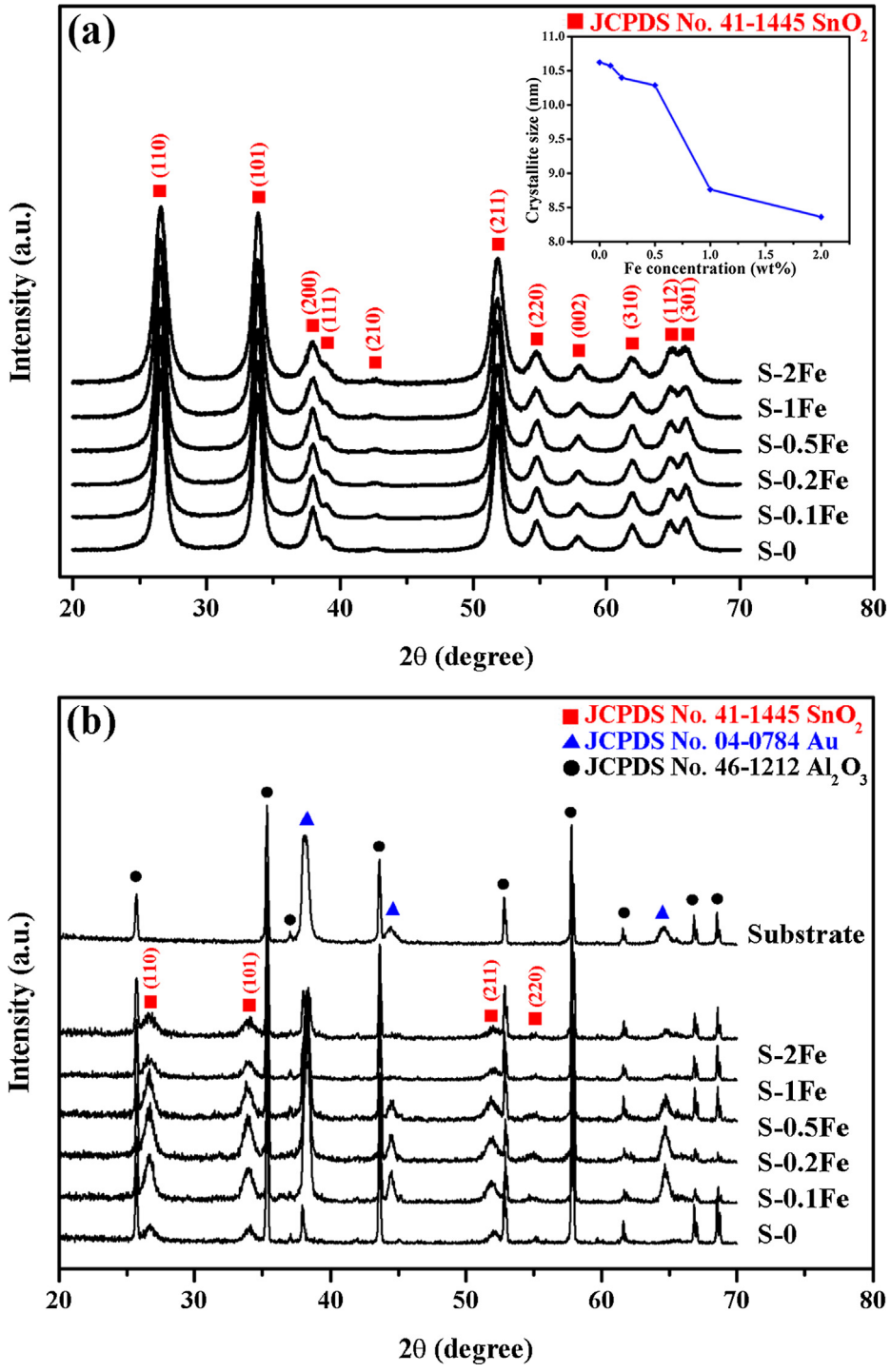

Fig. 1 XRD data of 0–2 wt% Fe-doped SnO_2 (a) nanoparticles (P-0 to P–2Fe) and (b) sensing films (S-0 to S–2Fe) after annealing and sensing test.

powders are only corresponding to the tetragonal cassiterite SnO_2 structure (JCPDS file No. 41-1445), indicating a single phase of highly crystalline SnO_2 material. In addition, all SnO_2 nanopowders show similar texturization with four major crystallographic planes at (1 1 0), (1 0 1), (2 1 1) and (2 0 0). Moreover, the peaks are slightly widened as the Fe-doping level rises from 0 to 2 wt%, implying the decrease of crystallite size. The crystallite sizes of nanoparticles calculated from Scherrer's equation is plotted as a function of Fe-doping concentration as embedded in Fig. 1(a). From the resulting plot, the average crystallite size slightly decreases as the Fe content rises from 0 to 0.5 wt% (~10.6 to ~10.3 nm) and then decreases rapidly from ~10.3 to ~8.4 nm as the Fe content increases additionally up to 2 wt%. Hence, the Fe dopants slightly limit grain enlargement of SnO_2 crystallites, which can be attributed to the strain-induced grain-diffusion barrier effect (Kim et al., 2007). The absence of Fe or Fe_2O_3 secondary peaks may be due to either the low amount of iron species or the development of the Fe-SnO_2 solid solution. Fig. 1(b) illustrates the related XRD patterns of all sensing films (S-0 and S-0.1Fe to S–2Fe) on Al_2O_3 substrates with Au/Cr electrodes after sensing test. It confirms similar crystallinity between the sensing films and their relevant powders having the same phase with no secondary phase of Fe or FeO_x. It can be noticed that the peaks of Au electrodes (JCPDS file No. 04-0784) and Al_2O_3 substrate (JCPDS file No. 46-1212) exhibit dominant magnitudes relative to those of sensing films due to high X-ray diffraction sensitivity of large-area Au interdigit patterns and large-grain Al_2O_3 crystallites of the substrate.

Fig. 2(a)–(d) illustrate typical bright field (BF)-TEM images with selected area electron diffraction (SAED) patterns (lower inset) and related high-resolution (HR)-TEM images (right zoom) of P-0, P-0.1Fe, P-0.5Fe and P–2Fe, respectively. All sample images demonstrate the primary particles with approximately round and polygonal shapes having various dimensions (3–20 nm). Additionally, the nanoparticles seem to be slightly smaller with increasing Fe-doping concentration and all particles appear to be the same phase, indicating the absence of iron or iron oxide secondary species. The relevant SAED patterns exhibit dotted ring features, specifying that particles are mainly semicrystalline with principal diffraction rings matched with principal planes of the cassiterite SnO_2 phase, in accordance with the perceived XRD data.

The related HR-TEM images shows various nanoparticles displaying lattice fringes, which can be indexed to principal planes of cassiterite SnO_2 phase. Additionally, the planes of P-2Fe tend to have slightly smaller *d*-spacing than those of P-0, P-0.1Fe and P-0.5Fe, signifying a smaller lattice constant due to substitutional doping of Fe atoms in the lattice. A replacement of Sn^{4+} by Fe^{3+} species should result in a reduced lattice constant due to its smaller ionic size (Bagheri-Mohagheghi et al., 2009; Kaur et al., 2012)) relative to that of Sn^{4+} (Lee et al., 2018; Sukunta et al., 2017; Kaur et al., 2012)). The Fe-Sn substitution is concordant with the Hume–Rothery principle due to the smaller difference of the Sn^{4+} and Fe^{3+} effective ionic radii than the upper bound of 15%. Besides, it agrees with some studies of Fe-doped SnO_2 nanomaterials, which indicate the conception of solid Fe-SnO_2 solution via the diffusion process (Bagheri-Mohagheghi et al., 2009; Beltran et al., 2010; Rao et al., 2017; Sambasivam et al., 2011).

The illustrative nitrogen adsorption–desorption isotherms with relevant pore size distributions (insets) of P-0, P-0.1Fe, P-0.5Fe and P-2Fe are exemplified in Fig. 3(a)–(d). It is observed that various isotherms similarly conform to the II-H3 IUPAC pattern, signifying the unhindered multilayer/monolayer adsorption on microporous-mesoporous adsorbents with capillary condensation (Sing et al., 1985). The

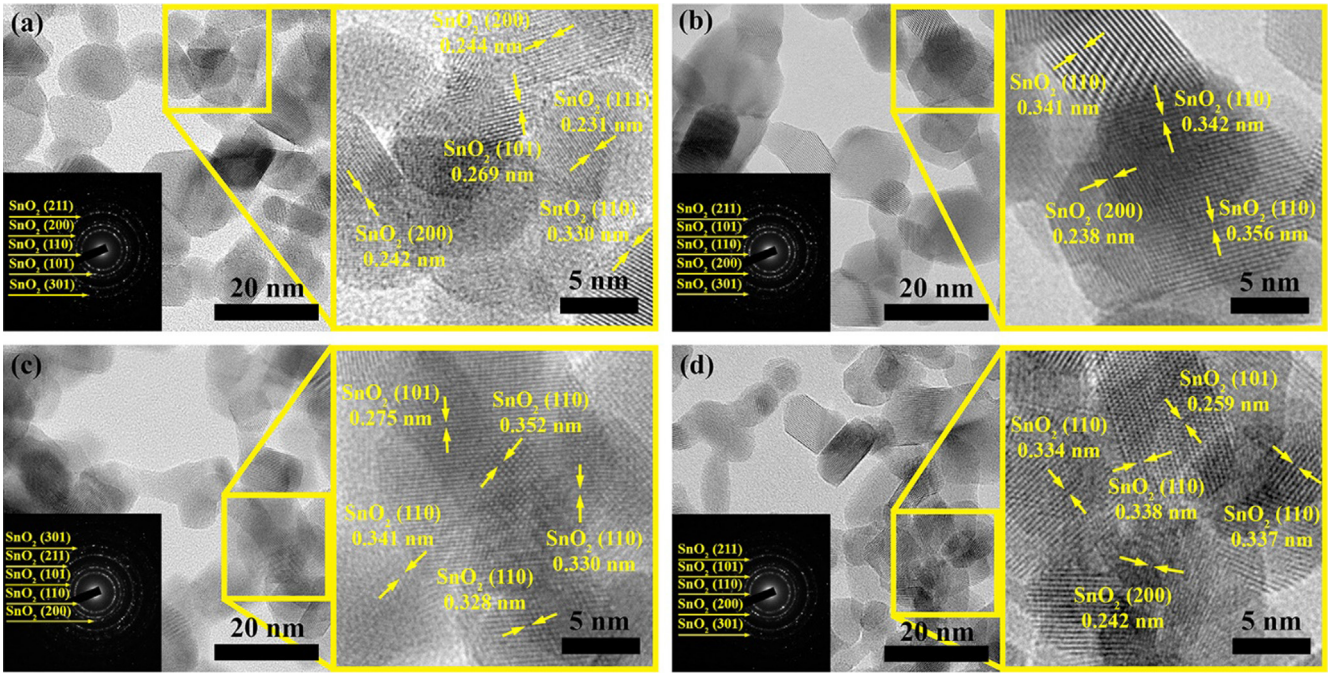

Fig. 2 BF-TEM images with SAED patterns (insets) and HR-TEM images of (a) undoped SnO_2 (P-0), (b) 0.1 wt% Fe-doped SnO_2 (P-0.1Fe), (c) 0.5 wt% Fe-doped SnO_2 (P-0.5Fe) and (d) 2 wt% Fe-doped SnO_2 nanoparticles (P-2Fe).

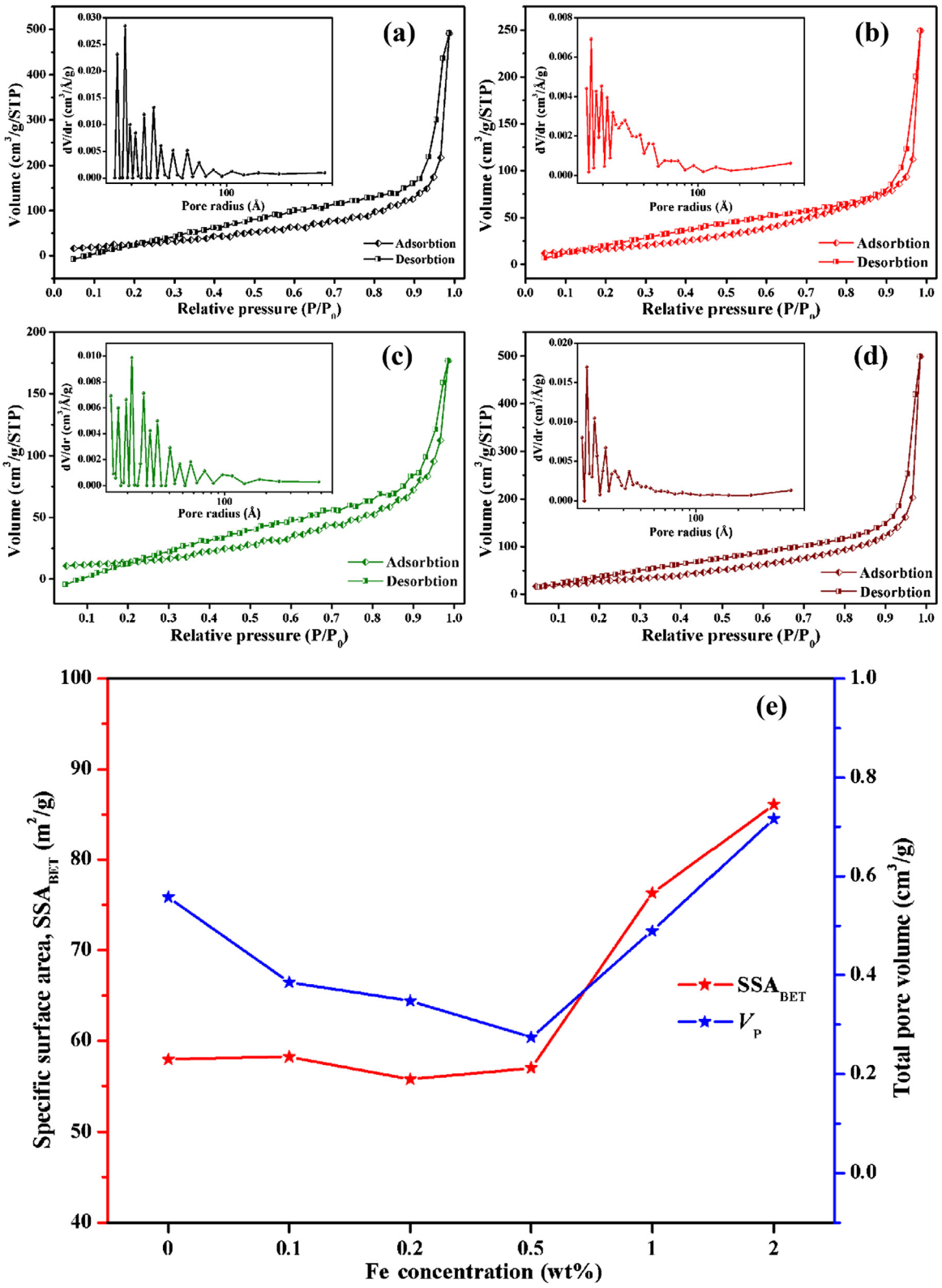

Fig. 3 N_2 adsorption isotherms with the corresponding BJH pore size distributions (insets) of (a) P-0, (b) P-0.1Fe, (c) P-0.5Fe and (d) P-2Fe. (e) Specific surface area: SSA_{BET} (red) and corresponding total pore volume: V_p (blue) vs. Fe content.

respective BJH pore size distributions further reveal the dependence of multi-mode pore size distribution on the Fe-doping content. The distribution of unloaded SnO_2 powder (P-0) displays two eminent maxima around 10–20 Å (Inset of Fig. 3(a)) but that of P-0.1Fe has one dominant maxima at ~15 Å (Insets of Fig. 3(b)). In the case of P-0.5Fe (Inset of Fig. 3(c)), the pore size distribution exhibits seven narrow peaks at the pore diameter of ~15, ~17, ~19, ~21, ~26, ~29 and ~ 32 Å, respec-

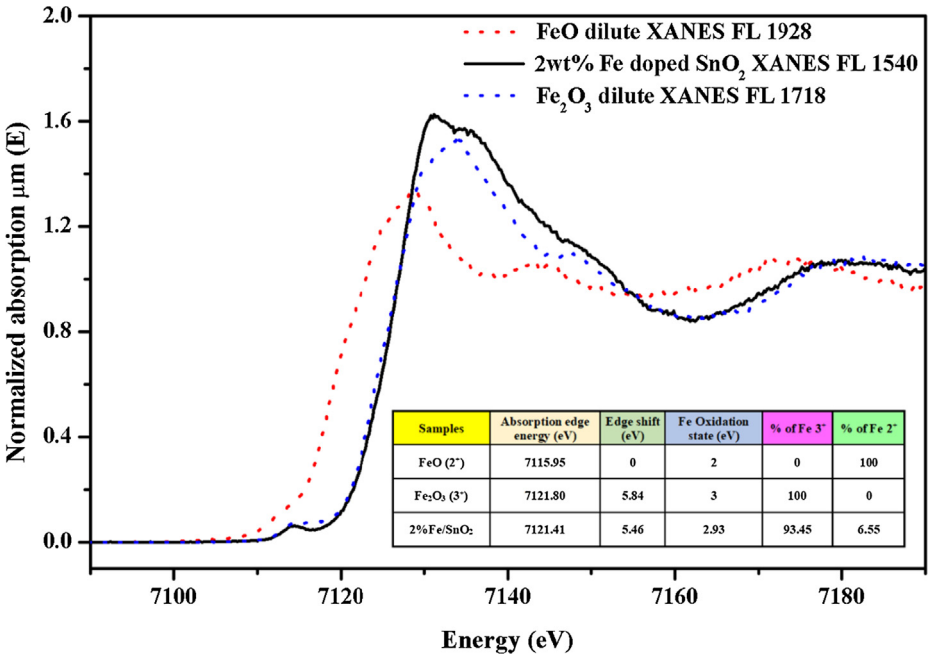

Fig. 4 XAS spectra of 2 wt% Fe-doped SnO_2, FeO and Fe_2O_3. Inset table: Estimated XAS parameters.

tively. At the highest Fe-doping level of 2 wt%, three notable peaks are seen ranging from ~15 to ~20 Å with one main maxima at ~16 Å. Also, the peak magnitudes of P-2Fe are considerably higher than those of P-0, P-0.1Fe and P-0.5Fe. The results imply that P-2Fe has relatively high micropore density relative to P-0, P-0.1Fe and P-0.5Fe while the Fe contents lower than 2 wt% result in the combination of micropores (< 20 Å) and mesopores (20–500 Å). In addition, the mesopore sizes tend to decrease with increasing Fe-doping concentration and the high Fe content results in higher pore density. Fig. 4(e) reports the BET specific surface area (SSA_{BET}) and total pore volume in relation to the Fe content. It can be seen that SSA_{BET} initially varies slightly as the Fe content rises from 0 to 0.5 wt% (around 57–58 m^2/g) but then increase markedly at the high Fe contents from 1 to 2 wt% (76.3–86.1 m^2/g). Similarly, the total pore volume decreases slowly from 0.56 to 0.27 cm^3/g as the Fe content increases from 0 to 0.5 wt% before increasing significantly to 0.72 cm^3/g when the Fe content additionally rises to 2 wt%. The large total pore volume and specific surface area may be associated with the very fine micropore features of the nanoparticle structure at high Fe contents.

The oxidation states and chemical species of Fe ions are determined from the standardized Fe K-edge XAS spectrum of 2 wt% Fe-doped SnO_2 nanoparticles relative to those of standard Fe compounds (FeO and Fe_2O_3) as demonstrated in Fig. 4. It is evident that the absorption edge of 2 wt% Fe-doped SnO_2 sample is located at 7121.41 eV, which lies much closer to that of Fe_2O_3 (7121.80 eV) compared with that of FeO (7115.95 eV). The relative percentage of Fe^{3+} and Fe^{2+} oxidation states are calculated by the interpolation of edge energies to be 93.45% and 6.55%, respectively as reported in the inset table (Fig. 4). Thus, the main oxidation state of Fe-doped flame-made SnO_2 nanoparticles is confirmed to be Fe^{3+}. It is also highly likely that Fe^{3+} states substitute Sn^{4+} ones in the lattice because the secondary phase of Fe_2O_3 cannot be observed according to the HR-TEM image.

Fig. 5 illustrates the high-resolution XPS spectra consisting of Sn 3d, Fe 2p and O 1 s principal levels of undoped and 2 wt% Fe-doped SnO_2 powders and sensors (P-0, S-0, P-2Fe and S-2Fe) after sensing test. For the Sn element, the spin-splitting pairs (Sn $3d_{5/2}$:Sn $3d_{3/2}$) of P-0 and P-2Fe (Fig. 5(a) and (c)) can be independently deconvoluted into the leading pairs located at 486.3:494.7 and 486.6:495.0 eV and the other minor pairs positioned at 487.1:495.7 and 487.8:496.1 eV, respectively. In contrast, the doublet pairs of S-0 and S-2Fe (Fig. 5(a) and (c)) can be fitted with individual doublet pairs of Gaussian peaks observed at 486.6:495.0 and 486.7:495.1 eV, respectively. The highest pairs of all samples can be associated with the same Sn^{4+} oxidation state (SnO_2) while the tiny pairs of P-0 or P-2Fe can match with the Sn^{4+} state of $Sn(OH)_4$ due to humidity adsorption (Kwoka et al., 2011). The results indicate that the states of Sn species are insignificantly affected by Fe-doping but depend on the form of materials. The materials in powder form contain Sn $(OH)_4$ species, which are absent in the related sensing films due possibly to humidity desorption after annealing and sensing test at elevated temperatures. Concerning the O element, the O 1s levels of P-0:P-2Fe (Fig. 5(b): (d)) can be similarly separated into four components peaked at 530.4:530.5 (main peak), 531.4:531.8, 532.3:532.8, and 533.2:534.1 eV, respectively. For the sensing films, the O 1s peak of S-0 (Fig. 5(b)) can be divided into three peaks centered at 530.1, 531.1 and 532.1 eV while that of S-2Fe (Fig. 5(d)) can be broken into four parts peaked at 530.4, 531.3, 532.5 and 533.9 eV, respectively. The major O 1s component can be attributed to surface lattice oxygen (O^{2-}) of Fe-doped SnO_2 structures while the minor ones located at 531.3–531.8, 532.5–532.8 and 533.9–534.1 eV may be attributed to the superoxide species (O_2^-), a hydroxyl (OH^-) group from humidity and loosely-bound oxygen molecules, respectively (Watts, 1994). The results suggest that the states of oxygen species are influenced by Fe doping and the Fe-doped SnO_2 samples tend to exhibit higher contents of chemisorbed and physisorbed oxygen species on

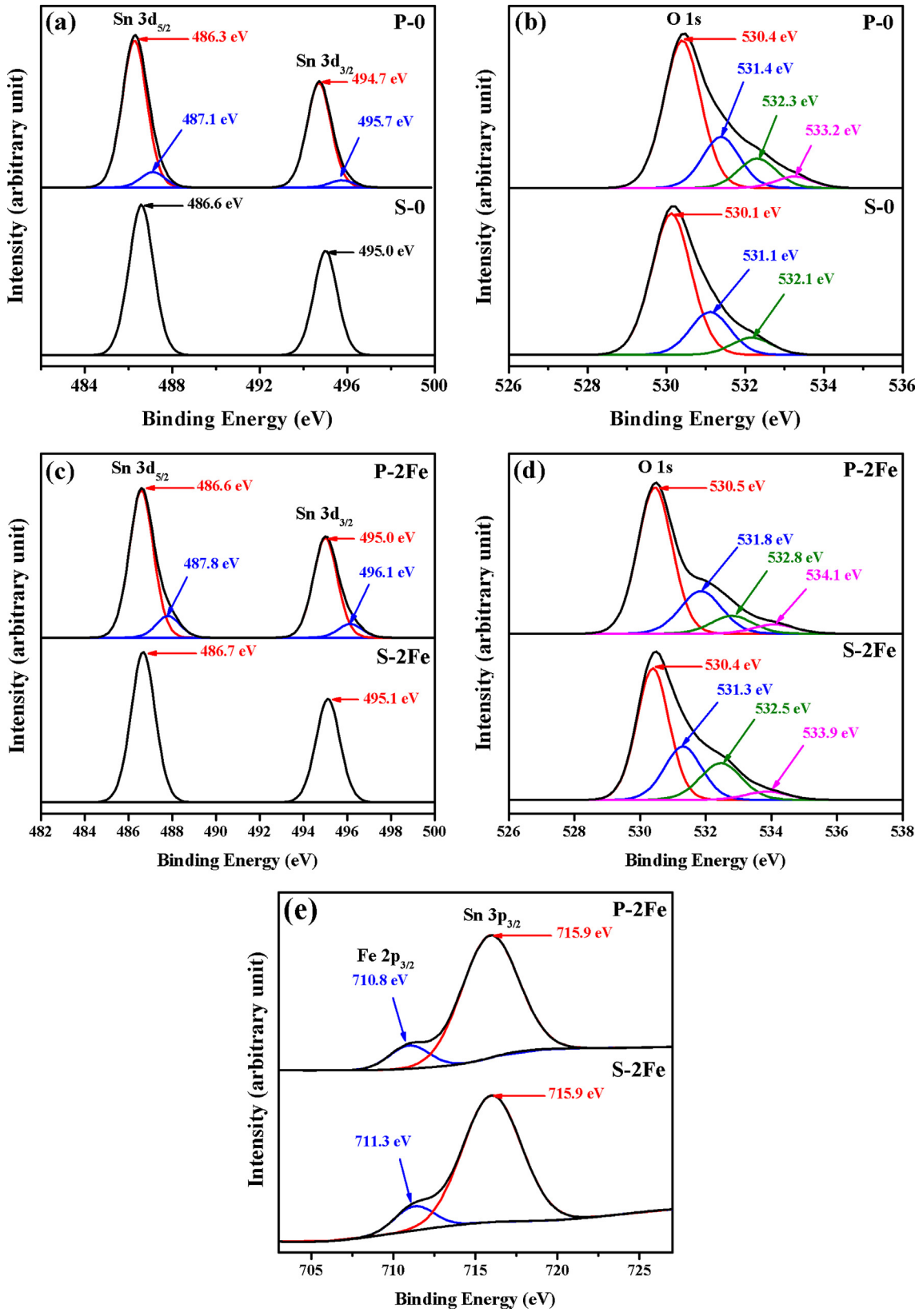

Fig. 5 High-energy resolution core-level XPS spectra of undoped and 2 wt% Fe-doped SnO_2 powders (P-0 and P-2Fe) and sensors (S-0 and S-2Fe): (a, c) Sn 3d, (b, d) O 1s and (e) Fe 2p.

surface. In the case of Fe element (Fig. 5(e)), the Fe 2p doublet pair overlaps with the Sn $3p_{3/2}$ peak of SnO_2 so that Fe 2p peaks must be found by the deconvolution of overlapped peaks. Due to relatively weak Fe 2p signals, only Fe $2p_{3/2}$ peaks of P-2Fe and S-2Fe can be found at 710.8 and 711.3 eV, respectively. They can match well with the Fe^{+3} oxidation state (Fe_2O_3) (Pradhan et al., 2014; Bhargava et al., 2007). The XPS result of Fe is in accordance with the Fe^{+3} oxidation state identified by XAS. It should be remarked that the XAS and XPS data of Fe-doped SnO_2 nanoparticles with lower Fe contents are omitted because their Fe signals are either poor or absent.

Fig. 6 shows UV–Vis absorption spectra of 0 – 2 wt% Fe-doped SnO_2 nanoparticles versus the wavelength in the range of 200–700 nm. It is seen that all samples show strong absorption edges in the UV region (300–330 nm) corresponding to the band gap transition and the edge position of Fe-doped SnO_2 nanoparticles moves toward longer wavelength as the Fe content rises from 0 to 2 wt%. The optical band gap energy (E_g) can then be calculated using Tauc's relation (Shaikh et al., 2017):

$$\alpha = C \times \frac{(h\nu - E_g)^n}{h\nu}$$

where C is a constant, α is the absorption coefficient taken from the UV-spectra, $h\nu$ is the photon energy and n is a constant depending on the type of transition: n = 1/2, 3/2, 2, and 3 for direct allowed, direct forbidden, indirect allowed, and indirect forbidden band gaps, respectively. The absorption data can be best fitted with n = 1/2, confirming the direct transition nature of SnO_2 semiconductor. Thus, the optical band gap of Fe-doped SnO_2 nanoparticles can be computed from the intercept of the extrapolated linear part (α = 0) of $(\alpha h\nu)^2$ versus $h\nu$ as displayed in the inset of Fig. 6. The band gap of P-0 (3.52 eV) is close to the reported values of SnO_2 materials prepared by various techniques (Saleh et al., 2016). With increasing Fe-doping content, the band gap energy decreases to 3.47, 3.44, 3.38, 3.16 and 2.95 eV for P-0.1Fe, P-0.2Fe, P-0.5Fe, P-1Fe and P-2Fe, respectively. The result reveals that

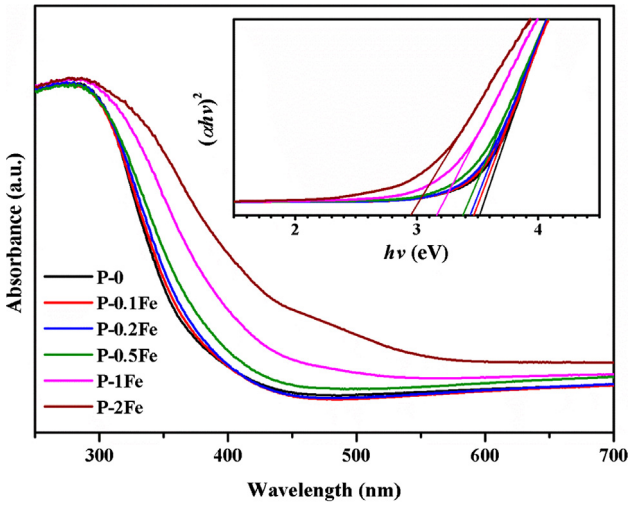

Fig. 6 UV–Visible absorbance spectra as a function of wavelength for SnO_2 nanoparticles with different Fe-doping levels. Inset: Tauc plots between $(\alpha h\nu)^2$ vs. photon energy.

the optical energy band gap decreases with increasing Fe content, which may be attributed to the doping effect of Fe atoms that introduces additional defect-state energy levels close to the band edges (Mani et al., 2017; Rao et al., 2017).

Fig. 7(a)–(f) demonstrate the cross-sectional SEM images of sensors (S-0 to S–2Fe) after sensing measurements. The images show various sensing films with thicknesses of ~10–15 μm comprising densely collective nanoparticles well arranged on solid alumina substrates. It was found that the densification of sensing films occurred after annealing at 450 °C. From the results, the Fe-doping level does not markedly affect the film density and the evenness of the film thickness endorses the reliability of powder-pasting and spin-coating methods.

3.2. Gas-sensing properties

The gas-sensing characteristics of SnO_2 sensors with different Fe concentrations were characterized in terms of sensor responses towards various environmental and flammable gases including C_2H_2, C_2H_5OH, H_2, CH_4, C_2H_4, H_2S, NH_3, CO_2, C_2H_4O, NO, NO_2 and N_2O at their typical concentrations and a working temperature of 300 °C as shown in Fig. 8. It is clear that the SnO_2 sensor (S-0) shows comparatively high response towards C_2H_5OH, modest responses to C_2H_2 and NO_2, and low responses to H_2, NH_3, CO_2, NO, H_2S, CH_4, C_2H_4O, C_2H_4 and N_2O, presenting good C_2H_5OH selectivity against these gases. With Fe-doping at the lowest content of 0.1 wt%, the C_2H_2 response increases prominently while those to C_2H_5OH, and NO_2 marginally decrease and other gas responses remain relatively very low. Thus, the small Fe-doping level causes the sensor to become selective to C_2H_2. However, the attained C_2H_2 selectivity is only guaranteed under the condition that the concentrations of C_2H_5OH and NO_2 polluting gases are usually in the ranges of lower than 1000 ppm and 10 ppm, respectively (Gouw et al., 2012; Bikov et al., 2013; Cho et al., 2006). Thus, the sensors will be applicable for C_2H_2 leakage detection under normal ambient conditions with typical polluting concentrations of C_2H_5OH and NO_2. As the Fe content additionally increases to 1 wt%, the C_2H_2 response decreases steadily but is still larger than those of other gases, implying reduced C_2H_2 selectivity. However, the NO_2 response decreases more significantly to a very low value at 1 wt% Fe, indicating improved C_2H_2 selectivity against NO_2 and the possible use of 1 wt% Fe-doped SnO_2 sensor for C_2H_2 detection when NO_2 is a potential interfering gas. With the highest Fe-doping level of 2 wt%, the responses to all gases degrade considerably to similar values and the sensor displays very low selectivity among these gases. From the data, the optimal Fe doping level of 0.1 wt% provides substantial improvement of C_2H_2-sensing characteristics at a moderate working temperature of 300 °C. Thus, only full results of C_2H_2 will be further reported.

C_2H_2 responses of all sensors (S-0 to S-2Fe) evaluated at different working temperatures from 200 to 350 °C towards 3 vol% C_2H_2 are displayed in Fig. 9. It is evident that all C_2H_2 responses monotonically rise with increasing temperature from 200 to 300 °C, before slightly reducing as the working temperature additionally increases to 350 °C. In addition, the response increases rapidly as the working temperature rises from 250 to 300 °C. Thus, the undoped and Fe-doped SnO_2 sensors (S-0 to S-2Fe) have the highest responses at the

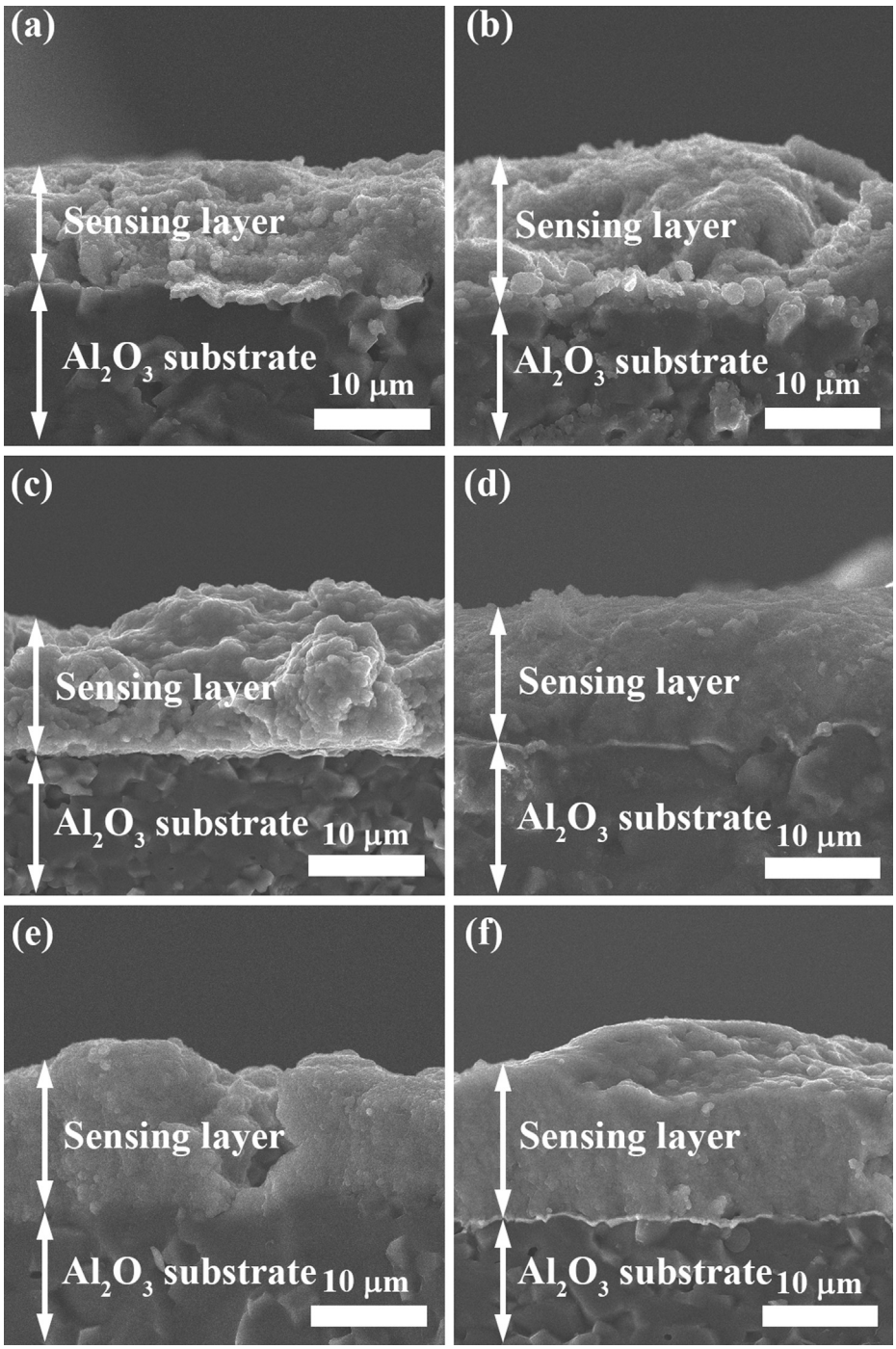

Fig. 7 SEM micrographs of undoped SnO_2 and Fe-doped SnO_2 sensing films: (a) S-0, (b) S-0.1Fe, (c) S-0.2Fe, (d) S-0.5Fe, (e) S-1Fe and (f) S–2Fe on Au/Al_2O_3 substrates.

optimal working temperature of 300 °C. Concerning the effect of Fe content, the sensor response increases greatly with a tiny Fe-doping level (0.1 wt%) while the higher Fe content leads to a substantial decline of C_2H_2 response. Principally, the S-0.1Fe sensor displays a high C_2H_2 response of ~750 to 3 vol% at 300 °C. The roles of Fe dopants and the influence of working temperature will be explained further in the mechanism section.

Fig. 10(a) displays the change in resistance of S-0 to S-2Fe sensors subjected to various C_2H_2 concentrations in backward (3–0.15 vol%) and forward (0.15–3 vol%) cycles at 300 °C. The results demonstrate that the resistance in air increases monotonically by more than a few orders of magnitude with increasing Fe content from 0 to 2 wt% and are repetitively stable in both cycles. Interestingly, the 0.1 wt% Fe-doped SnO_2 sensor exhibits notably rapid resistance decrease upon C_2H_2 exposure, confirming a common *n*-type gas-sensing property to a reducing gas. Furthermore, the change in resistance extends markedly with Fe-doping at the lowest content of 0.1 wt% but then deteriorates at higher Fe concentrations.

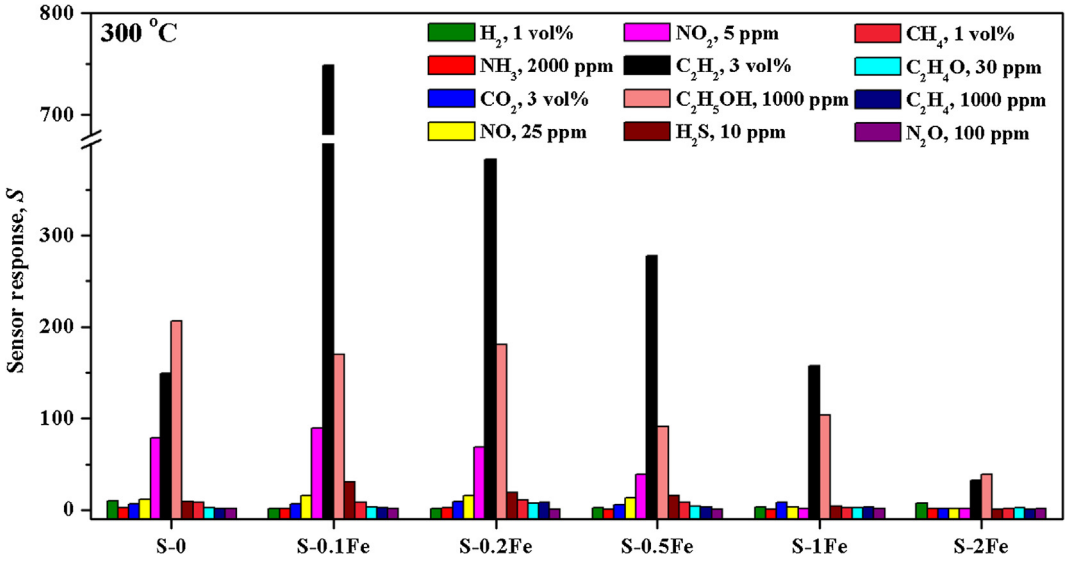

Fig. 8 The histogram of various gas responses including 1 vol% H_2, 2000 ppm NH_3, 3 vol% CO_2, 25 ppm NO, 5 ppm NO_2, 3 vol% C_2H_2, 1000 ppm C_2H_5OH, 10 ppm H_2S, 1 vol% CH_4, 30 ppm C_2H_4O, 1000 ppm C_2H_4 and 100 ppm N_2O at 300 °C of Fe-doped SnO_2 sensing films with various Fe-doping levels.

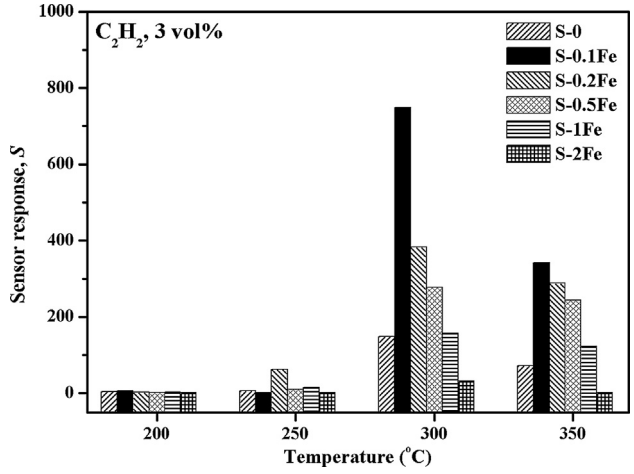

Fig. 9 The histogram of sensor response of 0–2 wt% Fe-doped SnO_2 sensing devices (S-0 to S-2Fe) to 3 vol% C_2H_2 as a function of operating temperature in the range of 200–350 °C.

The related sensor responses and responses time of all sensors (S-0 to S-2Fe) as functions of C_2H_2 concentration at 300 °C are reported in Fig. 10(b). It is clear that the C_2H_2 response critically increases owing to the addition of Fe at the small doping concentration of 0.1 wt% but then continually declines as the Fe concentration rises from 0.1 to 2 wt%. Particularly, the optimal Fe-doped sensor (S-0.1Fe) offers excellent responses of 741.0 (backward) and 748.7 (forward) with a small response time (~2.5 s) to 3 vol% C_2H_2 in comparison with S-0.2Fe (S = 376–383, t_{res} = ~3.1 s), S-0.5Fe (S = 277–282, t_{res} = ~3.5 s), S-1Fe (S = 154–158, t_{res} = ~5.3 s), S-0 (S = 125–143, t_{res} = ~61 s) and S-2Fe (S = 26–32, t_{res} = ~113 s), respectively. Regarding the gas response function, the responses rise steadily with increasing C_2H_2 concentration following the typical power-law relationships as reported along with the labels. It can be observed that the calculated exponent values in backward and forward cycles of all sensors are similarly around one, signifying that the amount of Fe dopants insignificantly affect the type of preadsorbed surface oxygen species (Yamazoe and Shimanoe, 2008). Moreover, the optimal Fe-doped sensor also displays good responses of 169–171 and 20–22 at lower concentrations of 1 and 0.15 vol%, respectively. Correspondingly, the limit of acetylene detection is estimated to be as low as ~25 ppm according the power equation at the threshold response of 1.1. Thus, the Fe-doped flame-made SnO_2 sensor is a potential candidate for leakage detection of acetylene, which is a widely used fuel for various industrial applications in cutting, welding, straightening and other confined heating processes (Lin et al., 2015). Furthermore, the achieved response and response time values are significantly better than other advanced C_2H_2 sensors as previously displayed in Table 1, which offer sensor response of < 70 and response time of > 3 s to C_2H_2 at various concentrations (< 1 vol%). The superior C_2H_2 sensing performances may be credited to relatively large effective surface area and well distributed Fe dopants in the FSP-made Fe-doped SnO_2 nanoparticles.

3.3. Gas-sensing mechanisms

From the observations, the optimum Fe-doping level of 0.1 wt % delivers significantly enhanced gas-sensing properties with high, fast and selective C_2H_2 response. However, the crystallite and particle sizes only slightly change upon Fe doping according to the structural characterization results. Hence, the slight change of morphology upon Fe doping should only marginally contribute to the response enhancement. Consequently, the catalytic and electronic effects of substitutional Fe dopants should play much more important roles to the gas-sensing enhancement, which can be described with the representations as portrayed in Fig. 11. With no Fe doping (Fig. 11(a)), the SnO_2 nanoparticles display nominal n-type behaviors with a moderate conductivity from n-type structural defects, which

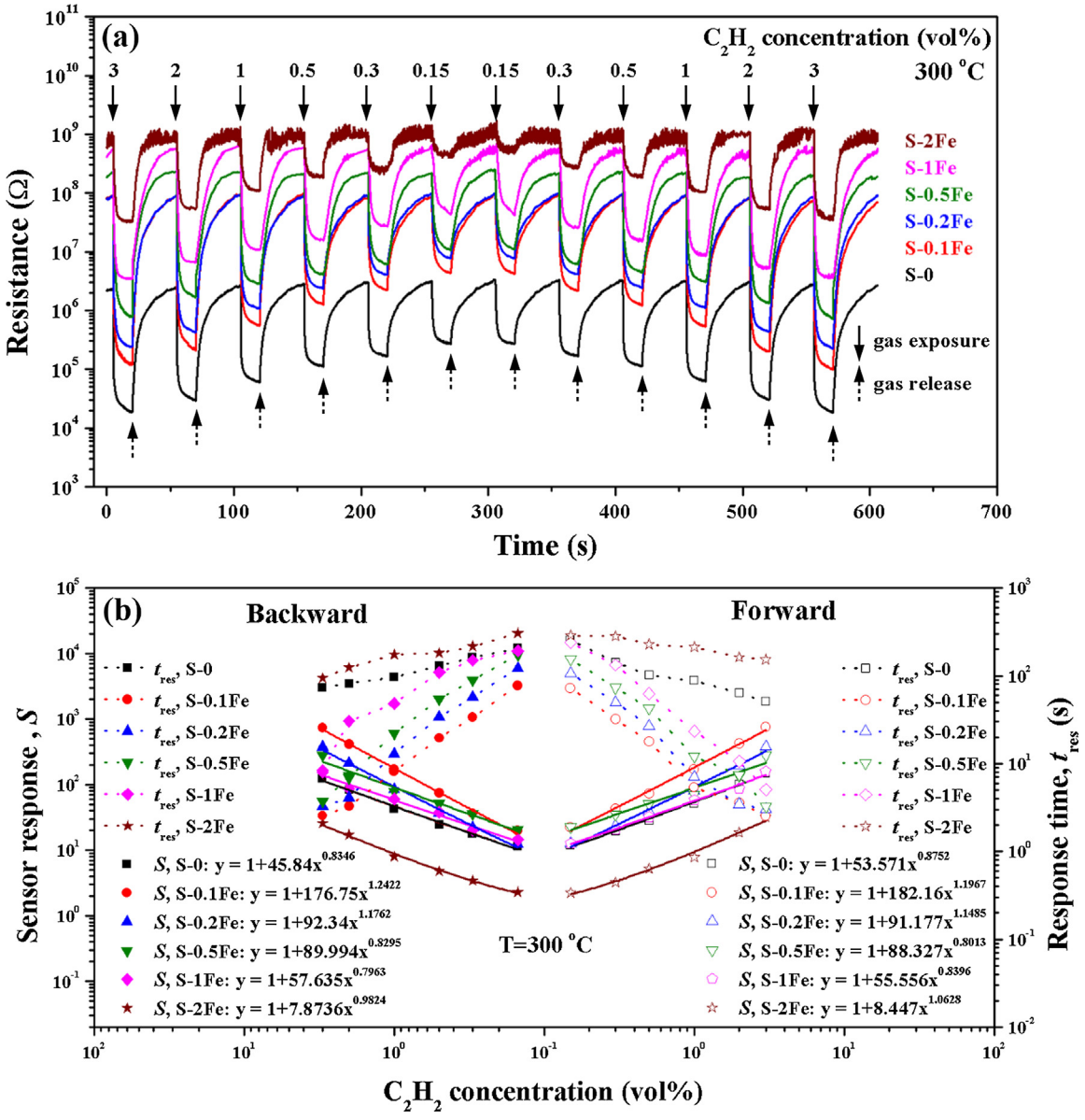

Fig. 10 (a) Change in resistance of 0–2 wt% Fe-doped SnO_2 sensors (S-0 to S-2Fe) subjected to 0.15–3 vol% C_2H_2 at 300 °C and (b) the relevant sensor response and response time vs. C_2H_2 concentration.

are mainly oxygen vacancies. SnO_2 has a relatively low electronic resistivity compared with many metal oxides owing to its relatively high amount of surface oxygen vacancies. On surface, chemisorbed oxygen species (O_2^-, O^- and O^{2-}) take electrons from SnO_2 conduction band and induce surface electron depletion regions as displayed in Fig. 11(a).

With Fe doping (Fig. 11(b)–(c)), Sn^{4+} ions in the lattice should be substituted by Fe^{3+} ions, resulting in the creation of holes via the defect reactions (Inyawilert et al., 2017):

$$Fe_2O_3 + \frac{1}{2}O_2 \rightarrow 2Fe'_{Sn} + 3O_o^x + V_o^{\cdot\cdot} \quad (1)$$

$$V_o^{\cdot\cdot} + \frac{1}{2}O_2 \rightarrow O_o^x + 2h^{\cdot} \quad (2)$$

where Fe_2O_3, Fe'_{Sn}, O_o^x, $h^{\cdot}$ and $V_o^{\cdot\cdot}$ are the quasi-Fe_2O_3 dopant molecule, the Fe-substituted Sn site having a single negative electronic charge, a neutral lattice oxygen site, a hole with a single positive electronic charge and oxygen vacancies with a double positive electronic charge, respectively. The induced holes will recombine with electrons, leading to a lower electron concentration and the extension of surface depletion regions. Thus, the resistance in air of SnO_2 nanoparticles rises significantly with increasing Fe doping content as observed earlier in Fig. 10(a). The assumption of Fe-Sn substitution is concordant with the results from TEM, XRD, XAS and XPS analyses. Additionally, it accords with the first principle determination of Fe-doped SnO_2 structure, which indicates the formation oxygen vacancies around Fe substitutional sites (Mudarra Navarro et al., 2015), resulting in hole generation upon interaction with O_2. Fe-doped SnO_2 materials will turn into *p*-type semiconductors if the hole concentration surpasses the electron concentration of SnO_2, and the resistance will be reducing with increasing Fe content (Galatsis et al., 2003;

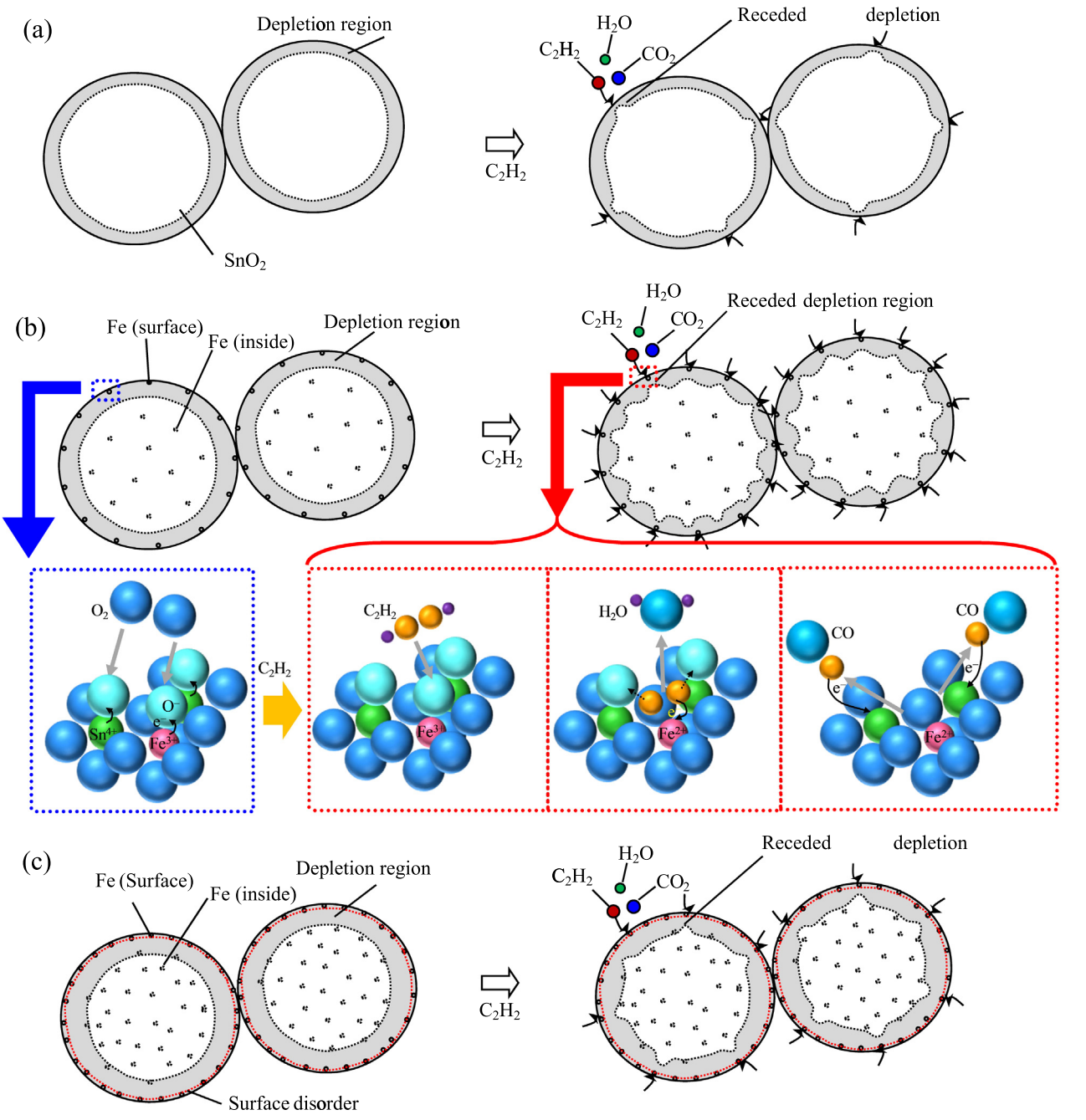

Fig. 11 Representations of C_2H_2 sensing process of SnO_2 nanoparticles with (a) no Fe doping, (b) Fe doping at an optimal concentration (0.1 wt%) with inset: the detailed atomic-level reaction mechanisms at a Fe^{3+} site and (c) Fe doping at a high concentration (> 0.1 wt%).

Othmen et al., 2016, 2018). Nonetheless, the gas-sensing data (Fig. 10(a)) reveal that the SnO_2 nanoparticles still display an *n*-type conductivity at the highest Fe content of 2 wt%. From the UV–Vis absorption analysis, the band gap energy decreases considerably from 3.52 to 2.95 eV as the Fe content increases from 0 to 2 wt%. This effect may lead to an increase of electron concentration via valence band to conduction band transition and lower resistance but the effect of *p*-type doping is dominant because the amount of these thermally excited electrons is much less than the hole concentration induced by the Fe dopants. After subjecting to C_2H_2, the chemisorbed oxygen species will interact with C_2H_2 molecules via the reaction paths:

$$C_2H_2 + 3O^-_{ads(SnO_2)} \rightarrow 2CO_{(g)} + H_2O_{(g)} + (SnO_2) + 3e^- \quad (3)$$

$$CO_{(ads)} + O^-_{ads(SnO_2)} \rightarrow CO_{2(g)} + e^- \quad (4)$$

$$C_2H_2 + 3O^{2-}_{ads(SnO_2)} \rightarrow 2CO_{(g)} + H_2O_{(g)} + (SnO_2) + 6e^- \quad (5)$$

$$CO_{(ads)} + O^{2-}_{ads(SnO_2)} \rightarrow CO_{2(g)} + 2e^- \quad (6)$$

To initiate the reactions, C_2H_2 molecules must adsorb and then be oxidized by O^- or O^{2-}, emancipating H_2O and CO. In addition, some CO may readsorb on surface and then oxidized again into CO_2. These processes reduce the steady-state surface coverage of oxygen species while releasing electrons into the SnO_2conduction band, leading to a lower electrical resistance. Hence, the C_2H_2 response will principally relate to the C_2H_2 dissociation rate and the amount of surface oxygen species. It can be expected that Fe doping can affect the C_2H_2 dissociation rates on SnO_2 since Fe and FeO_x are well-known catalysts for C_2H_2 dissociation widely used for the growth of nanocarbon materials (Khedr et al., 2008). In addition, Fe/SnO_2 cocatalysts have been used to synthesize carbon nanocoils from C_2H_2 source (Muneaki and Khalid, 2014). It is thus plausible that Fe-substituted SnO_2 nanoparticles can act as cocatalysts that will directly enhance C_2H_2 interaction as well as chemisorption of oxygen species as suggested by the XPS analysis discussed earlier.

The catalytic properties of Fe/SnO_2 cocatalysts for C_2H_2 detection can be quantitatively verified by considering the response rates versus Fe concentration using the Langmuir isotherm model (Boontum et al., 2018). According to the model, the adsorbed surface coverage of gas species will rise approximately linearly with increasing gas concentration at low gas concentrations or low partial gas pressures. In addition, the coverage is proportionate to the response rate at which oxygen species interact with gas molecules. The response rate corresponds to the rate of change in resistance and is the reciprocal of the response time (t_{res}^{-1}) (Singkammo et al., 2018). Fig. 12 displays the plots of t_{res}^{-1} versus C_2H_2 concentration of Fe-doped SnO_2 sensors with various Fe contents at 300 °C in forward and backward cycles. The results demonstrate that all sensor response rates for both cycles increase approximately linearly with increasing C_2H_2 concentration, following the Langmuir isotherm model. The slope of each plot corresponds to the effective reaction rate constant (k), which is plotted versus Fe concentration as presented in the inset of Fig. 12. It is apparent that the rate constant increases significantly to a maximum value at the optimal Fe content of 0.1 wt% before dropping rapidly down almost to the starting value as the Fe content increases to 2 wt%. The complex relationship of the rate constant with the Fe content signifies compound catalytic mechanisms of Fe-doped SnO_2 cocatalyst, which accelerates the reducing reaction with C_2H_2 via multi-step electron transfers (Natkaeo et al., 2018).

The exact catalytic roles of Fe dopants on gas-sensing mechanisms of SnO_2 materials remain not clearly understood and presently under exploration. In this research, a new C_2H_2 dissociation mechanism on Fe-doped SnO_2 surface is proposed with the atomic-level reaction models as sketched in the inset of Fig. 11(b). The first step illustrates the Fe-doped SnO_2 surface with preadsorbed oxygen species on Fe^{3+} and Sn^{4+} in air. Upon injecting acetylene, the C_2H_2 molecule may preferentially adsorb at Fe^{3+} sites of Fe-doped SnO_2 surface possibly by exchanging with the oxygen ion (O^-) and forming C_2 species together with a water molecule while an electron is injected to reduce Fe^{3+} to Fe^{2+}. Next, the oxidation of a C_2 molecule necessarily occurs via the interactions between two adjacent O^- species, resulting in the break of carbon triple bonds and the formation of pairs of CO molecules that may either directly desorb or readsorb to other sites and be oxidized again into CO_2 (omitted in the inset diagram). In the process, the oxidation of C_2 is expected to be the rate-limiting stage since the oxidation of C_2 into CO is a highly exothermic process (Ard et al., 2013). At this step, electrons are released back to Sn lattice to oxidize C_2 into CO molecules. The Fe^{3+} state will only be restored after readsorption of oxygen species. The low C_2H_2 response of undoped SnO_2 is likely due to a dissimilar role played by Sn compared with Fe on the formation of carbide. Iron carbide (FeC_x) can be much more easily formed compared with tin carbide (SnC_x) due to much lower required energy and temperature (H, 1896; Janbroers et al., 2011). Therefore, Fe-doping significantly improves the C_2H_2 response of SnO_2 nanoparticles by facilitating the carbon binding and succeeding oxidation of carbon species.

Moreover, the catalytic reactivity of Fe-doped SnO_2 nanostructures is rather particular to C_2H_2 molecules, resulting in high C_2H_2 selectivity against various oxidizing and reducing gases except ethanol (C_2H_5OH) due to their similar chemical structure and NO_2 due to its very high reactivity with SnO_2.

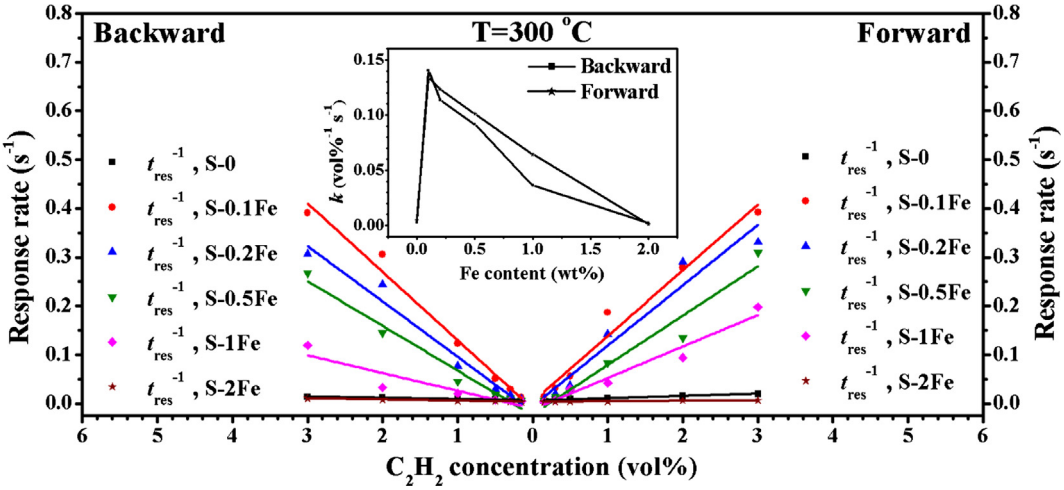

Fig. 12 Dependence of the sensor response rate on C_2H_2 concentration. Inset the effective reaction rate constant (k) versus the Fe concentration at 300 °C.

With increasing Fe content from 0 to 0.1 wt%, the high activity of Fe species provides enhanced C_2H_2 response but other gas responses are not much changed owing to their little reactivity with the nanoparticles. The attained selectivity may be associated with an optimal Fe-substituted Sn structure providing most suitable adsorption sites for C_2H_2. The activity of Fe/SnO_2 cocatalyst should depend significantly on the density of Fe sites in SnO_2 since the adsorption energy will be substantially affected by atoms surrounding the adsorption sites (Ard et al., 2013). At higher Fe-doping levels, the catalytic reactivity to C_2H_2 of Fe-doped SnO_2 nanostructures decreases rapidly due possibly to the elevating level of structural disorders particularly on surface whereas other gas responses also decrease but with lower rates because their reactivity were already low, leading to relatively low C_2H_2 selectivity. The disorders behave as surface states that capture charge carries (Zhang and Yin, 2013), reducing charge transfer from reducing or oxidizing reaction to the SnO_2 conduction band, lowering the change of surface conductivity and diminishing gas response as depicted in Fig. 11(c). Consequently, the response is optimal at a low Fe content of 0.1 wt% since active Fe^{3+} species are formed with a sufficiently low content of surface and bulk defects. At a higher Fe content, the sensor response declines due to increasing density of surface states. Nevertheless, additional experimental and theoretical studies of C_2H_2 interaction with Fe-doped SnO_2 nanostructures will be required to validate the offered mechanisms and conclude the true role of Fe dopant on the C_2H_2 sensing process.

Concerning the formation of oxygen species, the oxygen chemisorption rate depends mostly on temperature and the physiochemical properties of base metal oxides, which may be modified by additives. Hence, the characteristics of oxygen desorption and adsorption rates of a sensing material at different temperatures dictate the temperature dependency of gas-sensing properties. For pristine SnO_2, O_2^- ions are prevailing below 160 °C and will start transforming to O^-/O^{2-} species above this temperature whereas the desorption of O_2^- and O^- or O^2 will follow while reducing the temperature under 150 and 560 °C, respectively (Yamazoe et al., 1979). Thus, undoped SnO_2 sensors usually show an optimal adsorption rates of O^- and O^2 at 300–350 °C. Consequently, adsorbed C_2H_2 molecules can increasingly react with oxygen species as the temperature increases up to 300 °C but the desorption of C_2H_2 as well as oxygen species will become significant at higher temperatures, resulting in the decline of C_2H_2 response. With Fe doping, Fe atoms as *p*-type dopants for SnO_2 can enhance the density of oxygen vacancies, facilitating the dissociation of oxygen gas molecules into oxygen atoms (Zhao et al., 2017), which can chemisorb easily on the surfaces at a raised temperature, resulting in a supplementary increase of response. However, the small amount of Fe dopants does not change the temperature dependency of adsorption/desorption behaviors of SnO_2 surface. Thus, the Fe-doped SnO_2 sensors still exhibit the same optimal working temperature of 300 °C.

4. Conclusions

In conclusion, the FSP-made Fe-doped SnO_2 nanostructures with varying Fe concentrations were carefully studied for C_2H_2 gas sensing. Analyses by TEM, SEM, XRD, BET, XAS and XPS demonstrated that Fe-doped SnO_2 nanoparticles with diameters of ~5–20 nm were polycrystalline with the nominal tetragonal SnO_2 phase. In addition, the results suggested that Fe^{3+} species were doped substitutionally into the SnO_2 lattice. The test results revealed that the Fe-doping at a low content of 0.1 wt% led to a significantly enhanced response of 748.7 to 3 vol% C_2H_2 with a decent response time of ~2.5 s at an optimal working temperature of 300 °C. Furthermore, the Fe-doped SnO_2 sensor offered good C_2H_2 selectivity against C_2H_5OH, NO_2, H_2, NH_3, CO_2, NO, H_2S, CH_4, C_2H_4O, C_2H_4 and N_2O. Moreover, the activities of Fe dopants were effectively explained on the principle of catalytic effect with a new mechanistic model. Therefore, the flame-made Fe-doped SnO_2 nanoparticles were attractive materials for highly sensitive and selective C_2H_2 detection.

Acknowledgements

The authors gratefully acknowledge the financial support from the CMU 50th Anniversary Ph.D. Grant from Chiang Mai University (PHD/019/2556), Graduate School, Department of Physics and Materials Science, Faculty of Science, Chiang Mai University, National Science and Technology Development Agency (NSTDA), National Research Council of Thailand (NRCT), the Thailand Research Fund (TRF: RSA6080014) and the National Research University (NRU) Project under the Office of the Higher Education Commission (CHE), Ministry of Education, Thailand. We also wish to thank Center of Excellence (CoE) in Materials Science and Technology, Chiang Mai University for financial support under the administration of Materials Science Research Center, Faculty of Science, Chiang Mai University. Additionally, the authors gratefully acknowledge the Thailand Research Fund for TRF Research Team Promotion Grant (RTA6180004). The special thanks should be given to the National Electronics and Computer Technology Center (NECTEC), Pathumthani, Thailand for sensor facilities.

References

Ard, S.G., Melko, J.J., Fournier, J.A., Shuman, N.S., Viggiano, A.A., 2013. Reactions of Fe^+ and FeO^+ with C_2H_2, C_2H_4, and C_2H_6: temperature-dependent kinetics. J. Phys. Chem. A 117, 10178–10185.

Bagheri-Mohagheghi, M.M., Shahtahmasebi, N., Alinejad, M.R., Youssefi, A., Shokooh-Saremi, M., 2009. Fe-doped SnO_2 transparent semi-conducting thin films deposited by spray pyrolysis technique: thermoelectric and p-type conductivity properties. Solid State Sci. 11, 233–239.

Beltran, J.J., Sánchez, L.C., Osorio, J., Tirado, L., Baggio-Saitovitch, E.M., Barrero, C.A., 2010. Crystallographic and magnetic properties of Fe-doped SnO_2 nanopowders obtained by a sol–gel method. J. Mater. Sci. 45, 5002–5011.

Bhargava, G., Gouzman, I., Chun, C.M., Ramanarayanan, T.A., Bernasek, S.L., 2007. Characterization of the "native" surface thin film on pure polycrystalline iron: a high resolution XPS and TEM study. Appl. Surf. Sci. 253, 4322–4329.

Bikov, A., Paschalaki, K., Logan-Sinclair, R., Horváth, I., Kharitonov, S.A., Barnes, P.J., Usmani, O.S., Paredi, P., 2013. Standardised exhaled breath collection for the measurement of exhaled volatile organic compounds by proton transfer reaction mass spectrometry. BMC Pulm. Med. 13, 43.

Boontum, A., Phokharatkul, D., Hodak, J.H., Wisitsoraat, A., Hodak, S.K., 2018. H_2S sensing characteristics of Ni-doped $CaCu_3Ti_4O_{12}$ films synthesized by a sol-gel method. Sens. Actuat. B Chem. 260, 877–887.

Chen, W., Zhou, Q., Gao, T., Su, X., Wan, F., 2013a. Pd-doped SnO_2-based sensor detecting characteristic fault hydrocarbon gases in transformer oil. J. Nanomater. 2013, 9.

Chen, W., Zhou, Q., Su, X., Xu, L., Peng, S., 2013b. Morphology control of tin oxide nanostructures and sensing performances for acetylene detection. Sensors Transducers 154, 195–200.

Cho, P.-S., Kim, K.-W., Lee, J.-H., 2006. NO_2 sensing characteristics of ZnO nanorods prepared by hydrothermal method. J. Electroceram. 17, 975–978.

Choi, K.S., Park, S., Chang, S.-P., 2017. Enhanced ethanol sensing properties based on SnO_2 nanowires coated with Fe_2O_3 nanoparticles. Sens. Actuat. B Chem. 238, 871–879.

Galatsis, K., Cukrov, L., Wlodarski, W., McCormick, P., Kalantar-zadeh, K., Comini, E., Sberveglieri, G., 2003. p- and n-type Fe-doped SnO_2 gas sensors fabricated by the mechanochemical processing technique. Sensors Actuat. B: Chem. 93, 562–565.

Gouw, J.A., Gilman, J.B., Borbon, A., Warneke, C., Kuster, W.C., Goldan, P.D., Holloway, J.S., Peischl, J., Ryerson, T.B., Parrish, D.D., Gentner, D.R., Goldstein, A.H., Harley, R.A., 2012. Increasing atmospheric burden of ethanol in the United States. Geophys. Res. Lett., 39

H, G.N., 1896. Metallic carbides. Nature 54, 357.

Inyawilert, K., Wisitsoraat, A., Tuantranont, A., Phanichphant, S., Liewhiran, C., 2017. Ultra-sensitive and highly selective H_2 sensors based on FSP-made Rh-substituted SnO_2 sensing films. Sens. Actuat. B Chem. 240, 1141–1152.

Janbroers, S., Crozier, P.A., Zandbergen, H.W., Kooyman, P.J., 2011. A model study on the carburization process of iron-based Fischer-Tropsch catalysts using in situ TEM–EELS. Appl. Catal. B 102, 521–527.

Jiao, Z., Wang, S., Bian, L., Liu, J., 2000. Stability of SnO_2/Fe_2O_3 multilayer thin film gas sensor. Mater. Res. Bull. 35, 741–745.

Kaur, J., Shah, J., Kotnala, R.K., Verma, K.C., 2012. Raman spectra, photoluminescence and ferromagnetism of pure, Co and Fe doped SnO_2 nanoparticles. Ceram. Int. 38, 5563–5570.

Khedr, M.H., Abdel Halim, K.S., Soliman, N.K., 2008. Effect of temperature on the kinetics of acetylene decomposition over reduced iron oxide catalyst for the production of carbon nanotubes. Appl. Surf. Sci. 255, 2375–2381.

Kim, S.G., Kim, W.T., Park, Y.B., 2007. Abnormal grain growth induced by boundary segregation of solute atoms. Mater. Sci. Forum 558–559, 1093–1099.

Kotchasak, N., Wisitsoraat, A., Tuantranont, A., Phanichphant, S., Yordsri, V., Liewhiran, C., 2018. Highly sensitive and selective detection of ethanol vapor using flame-spray-made CeO_x-doped SnO_2 nanoparticulate thick films. Sens. Actuat. B Chem. 255, 8–21.

Kwoka, M., Waczyńska, N., Kościelniak, P., Sitarz, M., Szuber, J., 2011. X-ray photoelectron spectroscopy and thermal desorption spectroscopy comparative studies of L-CVD SnO_2 ultra thin films. Thin Solid Films 520, 913–917.

Lee, I.-J., Park, J., Sung, N.-E., Kim, J., 2018. X-ray absorption fine structure investigation of the local structure of SnO_2-doped ZnO films. Mater. Chem. Phys. 206, 103–109.

Li, Y., Hu, Y., Jiang, H., Hou, X., Li, C., 2013. Construction of core-shell $Fe_2O_3@SnO_2$ nanohybrids for gas sensors by a simple flame-assisted spray process. RSC Adv. 3, 22373–22379.

Liewhiran, C., Tamaekong, N., Wisitsoraat, A., Phanichphant, S., 2012. Highly selective environmental sensors based on flame-spray-made SnO_2 nanoparticles. Sens. Actuat. B Chem. 163, 51–60.

Liewhiran, C., Tamaekong, N., Wisitsoraat, A., Tuantranont, A., Phanichphant, S., 2013. Ultra-sensitive H_2 sensors based on flame-spray-made Pd-loaded SnO_2 sensing films. Sens. Actuat. B Chem. 176, 893–905.

Lin, Y., Li, C., Wei, W., Li, Y., Wen, S., Sun, D., Chen, Y., Ruan, S., 2015. A new type of acetylene gas sensor based on a hollow heterostructure. RSC Adv. 5, 61521–61527.

Mani, R., Vivekanandan, K., Subiramaniyam, N.P., 2017. Photocatalytic activity of different organic dyes by using pure and Fe doped SnO_2 nanopowders catalyst under UV light irradiation. J. Mater. Sci.: Mater. Electron. 28, 13846–13852.

Mudarra Navarro, A.M., Rodríguez Torres, C.E., Cabrera, A.F., Weissmann, M., Nomura, K., Errico, L.A., 2015. Ab initio study of the ferromagnetic response, local structure, and hyperfine properties of Fe-doped SnO_2. J. Phys. Chem. C 119, 5596–5603.

Muneaki, H., Khalid, L., 2014. Synthesis and growth kinetics of carbon nanocoils using Sn-Fe-O xerogel film catalyst. Mater. Res. Express 1. 035027.

Natkaeo, A., Phokharatkul, D., Hodak, J.H., Wisitsoraat, A., Hodak, S.K., 2018. Highly selective sub–10 ppm H_2S gas sensors based on Ag-doped $CaCu_3Ti_4O_{12}$ films. Sens. Actuat. B Chem. 260, 571–580.

Othmen, W.B.H., Hamed, Z.B., Sieber, B., Addad, A., Elhouichet, H., Boukherroub, R., 2018. Structural and optical characterization of p-type highly Fe-doped SnO2 thin films and tunneling transport on SnO2:Fe/p-Si heterojunction. Appl. Surf. Sci. 434, 879–890.

Othmen, W.B.H., Sdiri, N., Elhouichet, H., Férid, M., 2016. Study of charge transport in Fe-doped SnO_2 nanoparticles prepared by hydrothermal method. Mater. Sci. Semicond. Process. 52, 46–54.

Pradhan, G.K., Reddy, K.H., Parida, K.M., 2014. Facile fabrication of mesoporous α-Fe_2O_3/SnO_2 nanoheterostructure for photocatalytic degradation of malachite green. Catal. Today 224, 171–179.

Punginsang, M., Wisitsora-at, A., Tuantranont, A., Phanichphant, S., Liewhiran, C., 2015. Effects of cobalt doping on nitric oxide, acetone and ethanol sensing performances of FSP-made SnO_2 nanoparticles. Sens. Actuat. B Chem. 210, 589–601.

Qi, Q., Zhang, T., Zheng, X., Fan, H., Liu, L., Wang, R., Zeng, Y., 2008. Electrical response of Sm_2O_3-doped SnO_2 to C_2H_2 and effect of humidity interference. Sens. Actuat. B Chem. 134, 36–42.

Rao, G.T., Babu, B., Ravikumar, R.V.S.S.N., Shim, J., Reddy, C.V., 2017. Structural and optical properties of Fe-doped SnO_2 quantum dots. Mater. Res. Express 4, 125021.

Righettoni, M., Tricoli, A., Pratsinis, S.E., 2010. Si:WO_3 Sensors for highly selective detection of acetone for easy diagnosis of diabetes by breath analysis. Anal. Chem. 82, 3581–3587.

Saleh, S.A., Ibrahim, A.A., Mohamed, S.H., 2016. Structural and optical properties of nanostructured Fe-doped SnO_2. Acta Phys. Pol. A 129, 1220–1225.

Sambasivam, S., Choi, B.C., Lin, J.G., 2011. Intrinsic magnetism in Fe doped SnO_2 nanoparticles. J. Solid State Chem. 184, 199–203.

Samerjai, T., Tamaekong, N., Wetchakun, K., Kruefu, V., Liewhiran, C., Siriwong, C., Wisitsoraat, A., Phanichphat, S., 2012. Flame-spray-made metal-loaded semiconducting metal oxides thick films for flammable gas sensing. Sens. Actuat. B Chem. 171–172, 43–61.

Shaikh, F.I., Chikhale, L.P., Patil, J.Y., Mulla, I.S., Suryavanshi, S.S., 2017. Enhanced acetone sensing performance of nanostructured Sm_2O_3 doped SnO_2 thick films. J. Rare Earths 35, 813–823.

Shan, H., Liu, C., Liu, L., Zhang, J., Li, H., Liu, Z., Zhang, X., Bo, X., Chi, X., 2013. Excellent toluene sensing properties of SnO_2–Fe_2O_3 interconnected nanotubes. ACS Appl. Mater. Interfaces 5, 6376–6380.

Sing, K.S.W., Everett, D.H., Haul, R.A.W., Moscou, L., Pierotti, R. A., Rouquerol, J., Siemieniewska, T., 1985. Reporting physisorption data for gas/solid systems with special reference to the determination of surface area and porosity. Pure Appl. Chem. 57, 603–619.

Singkammo, S., Wisitsoraat, A., Sriprachuabwong, C., Tuantranont, A., Phanichphant, S., Liewhiran, C., 2015. Electrolytically exfoliated graphene-loaded flame-made Ni-doped SnO_2 composite film for acetone sensing. ACS Appl. Mater. Interfaces 7, 3077–3092.

Singkammo, S., Wisitsoraat, A., Tuantranont, A., Phanichphant, S., Yodsri, V., Liewhiran, C., 2018. Catalytic roles of Sm2O3 dopants

on ethylene oxide sensing mechanisms of flame-made SnO_2 nanoparticles. Appl. Surf. Sci. 454, 30–45.

Sukunta, J., Wisitsoraat, A., Tuantranont, A., Phanichphant, S., Liewhiran, C., 2017. Highly-sensitive H 2 S sensors based on flame-made V-substituted SnO_2 sensing films. Sens. Actuat. B Chem. 242, 1095–1107.

Sun, P., Cai, Y., Du, S., Xu, X., You, L., Ma, J., Liu, F., Liang, X., Sun, Y., Lu, G., 2013. Hierarchical α-Fe_2O_3/SnO_2 semiconductor composites: Hydrothermal synthesis and gas sensing properties. Sens. Actuat. B Chem. 182, 336–343.

Vuong, D.D., Trung, K.Q., Hung, N.H., Hieu, N.V., Chien, N.D., 2014. Facile preparation of large-scale α-Fe_2O_3 nanorod/SnO_2 nanorod composites and their LPG-sensing properties. J. Alloys Compd. 599, 195–201.

Watts, J.F., 1994. X-ray photoelectron spectroscopy. Vacuum 45, 653–671.

Yamazoe, N., Fuchigami, J., Kishikawa, M., Seiyama, T., 1979. Interactions of tin oxide surface with O_2, H_2O AND H_2. Surf. Sci. 86, 335–344.

Yamazoe, N., Shimanoe, K., 2008. Theory of power laws for semiconductor gas sensors. Sens. Actuat. B Chem. 128, 566–573.

Yu, Q., Zhu, J., Xu, Z., Huang, X., 2015. Facile synthesis of α-Fe_2O_3@SnO_2 core–shell heterostructure nanotubes for high performance gas sensors. Sens. Actuat. B Chem. 213, 27–34.

Zhang, L., Yin, Y., 2013. Large-scale synthesis of flower-like ZnO nanorods via a wet-chemical route and the defect-enhanced ethanol-sensing properties. Sens. Actuat. B Chem. 183, 110–116.

Zhao, X., Wen, T., Zhang, J., Ye, J., Ma, Z., Yuan, H., Ye, X., Wang, Y., 2017. Fe-Doped SnO_2 catalysts with both BA and LA sites: facile preparation and biomass carbohydrates conversion to methyl lactate MLA. RSC Adv. 7, 21678–21685.

Zhou, Q., Cao, M., Li, W., Tang, C., Zhu, S., 2015. Research on acetylene sensing properties and mechanism of SnO_2 based chemical gas sensor decorated with Sm_2O_3. J. Nanotechnol. 2015, 1–7.